



One-dimensional $\text{Mg}_x\text{Ti}_y\text{O}_x + 2y$ nanostructures: General synthesis and enhanced photocatalytic performance

Guorui Yang^{a,b}, Ling Wang^a, Yanmei Zhao^c, Shengjie Peng^{b,d,**}, Jianan Wang^a, Dongxiao Ji^b, Zhe Wang^b, Wei Yan^{a,*}, Seeram Ramakrishna^b

^a Department of Environmental Science & Engineering, State Key Laboratory of Multiphase Flow in Power Engineering, Xi'an Jiaotong University, Xi'an 710049 China

^b Department of Mechanical Engineering, National University of Singapore, 117574 Singapore

^c Department of Computer Science, National University of Singapore, 117417 Singapore

^d Jiangsu Key Laboratory of Materials and Technology for Energy Conversion, College of Materials Science and Technology, Nanjing University of Aeronautics and Astronautics, Nanjing 210016, China

ARTICLE INFO

Keywords:

MgTi_2O_5
Electrospinning
General synthesis
Nanofiber
Hydrogen

1. Introduction

Photocatalytic hydrogen evolution from water splitting employing semiconductor as photocatalysts provides a promising strategy for solar energy conversion and a prospect of replacing fossil fuels [1–3]. As is generally known, the further practical utilization of this technology is to a large extent relied on the significant development of photocatalysts with satisfactory performance [4]. Alkali titanates, as a stable photocatalysts for water splitting, were research hotspots [5,6]. In particular, the alkali titanates possessed a more negative conduction band and better stability compared with the most studied TiO_2 [7–10], which are the favorable features for efficient water splitting. In addition, the photocatalysts of alkali titanates tended to contain oxygen vacancies and M vacancies because of their intrinsic non-stoichiometric ratio, which could boost the separation efficiency of the photoinduced electron/hole (e^-/h^+) pairs and facilitate the migration of charge carriers from the volume to the surface [11].

$\text{Mg}_x\text{Ti}_y\text{O}_x + 2y$, as important members in the family of alkali titanates, has proven to be multi-functional materials, which extensively explored as ceramic capacitor [12], resonator [13], photocatalyst [14–16], anodes for metal (including Li, Na and Mg)-ion batteries [17–19], absorbent for heavy metal-ion elimination [20] and so on [21–25]. Especially, the MgTi_2O_5 and its derived heterostructures recently exhibited prospect in the application of photocatalysis, because

of their suitable electronic structure and conduction band position matching well with the redox potential for water splitting [26–28]. Zhang et al. [26] investigated the photocatalytic water splitting performance of pure MgTi_2O_5 nanoparticles. Ehsan et al. [27] also fabricated MgTi_2O_5 microparticles that displayed good photoelectrical activity. Qu et al. [8] reported that the $\text{MgTiO}_3/\text{MgTi}_2\text{O}_5$ heterogeneous nanorods exhibited high efficiency of photocatalytic hydrogen production. However, steerable synthesis of $\text{Mg}_x\text{Ti}_y\text{O}_x + 2y$ with pure phase as well as modulated morphologies is still a huge challenge that have restricted its further applications. As indicated in the previous literature [26], the pure phase MgTi_2O_5 was hard to be prepared in practice, due to associated minerals of MgTiO_3 and Mg_2TiO_4 .

One-dimensional (1D) nanostructures have currently garnered a flourish of interest in the fields of nanoscale science and technology, mainly owing to their wide range of applications basically benefiting from their desirable thermal, optical, electronic and magnetic properties [29–31]. Specially, the diffusion coefficient of the photoinduced electrons in 1D nanostructures is several orders of magnitude higher than that in nanoparticulate structures, which convincingly promotes the photocatalytic activity [32]. In this regard, the 1D $\text{Mg}_x\text{Ti}_y\text{O}_x + 2y$ nanostructures deserve the expectation of delivering higher photocatalytic activity. More importantly, the 1D $\text{Mg}_x\text{Ti}_y\text{O}_x + 2y$ nanostructures can be further served as substrates to build more complicate heterostructures as more efficient photocatalysts under solar light

* Corresponding author.

** Corresponding author at: Department of Mechanical Engineering, National University of Singapore, 117574 Singapore.

E-mail addresses: sjpeng@nus.edu.sg (S. Peng), yanwei@xjtu.edu.cn (W. Yan).

conditions. Nevertheless, to the best of our knowledge, reports covering the fabrication of $\text{Mg}_x\text{Ti}_y\text{O}_{x+2y}$ nanofibers and detailed investigations on their performance over photocatalytic H_2 evolution yet are comparatively scarce. Herein, we successfully fabricated a series of 1D $\text{Mg}_x\text{Ti}_y\text{O}_{x+2y}$ including MgTi_2O_5 , MgTiO_3 and Mg_2TiO_4 , nanofibers with pure phase by a facile electrospinning technique [33,34]. Compared with the nanoparticle counterpart, such 1D nanostructures displayed excellent activity over photocatalytic hydrogen evolution from water splitting.

2. Experimental section

2.1. Chemicals and materials

Magnesium acetate [$\text{Mg}(\text{CH}_3\text{COO})_2 \cdot 4\text{H}_2\text{O}$], tetra-*n*-butyl titanate [$\text{Ti}(\text{OC}_4\text{H}_9)_4$], acetic acid (CH_3COOH), methyl alcohol (CH_3OH), sodium sulfide (Na_2S) and sodium sulfite (Na_2SO_3) were purchased from Sinopharm Chemical Reagent Co., Ltd. Poly (vinylpyrrolidone) (PVP, $\text{Mw} \approx 1.3 \times 10^6$) was purchased from BASF chemical company in Germany. Degussa P25 was produced by Degussa AG Company in Germany. All chemicals were used as received.

2.2. Fabrication of $\text{Mg}_x\text{Ti}_y\text{O}_{x+2y}$ nanofibers

$\text{Mg}(\text{CH}_3\text{COO})_2 \cdot 4\text{H}_2\text{O}$ and $\text{Ti}(\text{OC}_4\text{H}_9)_4$ with molar ratio of 1:2 were dissolved in a mixture of CH_3OH and CH_3COOH (weight ratio 4:1), then the solution was stirred at room temperature for about 6 h to form a clean solution (Fig. S1 step 1). 10 mL of the precursor solution was loaded into a syringe with a stainless steel needle connected to a high-voltage supply. A voltage of 12 kV was used for the spinneret. A sheet of aluminum foil was used as the collector and placed 12 cm away from the needle (Fig. S1 step 2). Finally, the as-spun fibers were calcined at 650°C for 4 h with a ramp rate of 2°C in air to obtain the pure MgTi_2O_5 nanofibers, denoted as $\text{MT}_2\text{-NF}$ (Fig. S1 step 3). For the preparation of MgTi_2O_5 nanoparticles (labelled as $\text{MT}_2\text{-NP}$), the sol-precursor solution was dried under vacuum at 60°C for 10 h to produce the gel layer. The dried gels were calcined at 650°C for 4 h. The MgTiO_3 and Mg_2TiO_4 nanofibers (denoted as MT-NF and $\text{M}_2\text{T-NF}$, respectively.) and nanoparticles (denoted as MT-NP and $\text{MT}_2\text{-NP}$, respectively.) were obtained by only tuning the ratios of Mg to Ti, under the same conditions via electrospinning and sol-gel routes, respectively. In particular, the molar ratio of $\text{Mg}(\text{CH}_3\text{COO})_2 \cdot 4\text{H}_2\text{O}$ to $\text{Ti}(\text{OC}_4\text{H}_9)_4$ were fixed at 1:1 and 2:1 for MgTiO_3 and Mg_2TiO_4 , respectively. In addition, the $\text{MgTi}_2\text{O}_5/\text{MgTiO}_3$ ($\text{MT}_2/\text{MT-NF}$) and $\text{Mg}_2\text{TiO}_4/\text{MgTiO}_3$ ($\text{MT}_2/\text{MT-NF}$) heterojunction nanofibers were also prepared at different molar ratio of $\text{Mg}(\text{CH}_3\text{COO})_2 \cdot 4\text{H}_2\text{O}$ to $\text{Ti}(\text{OC}_4\text{H}_9)_4$ which were of 1:1.5 and 1.5:1, respectively.

2.3. Characterization

Scanning electron microscopy (SEM) micrographs were taken using a JEOL JSM 6700F instrument, and energy-dispersive X-ray spectrum (EDS) was executed on JEOL JSM 6460. The transmission electron microscopy (TEM) observation was performed on a JEOL JEM-2100 electron microscope with an acceleration voltage of 200 kV. X-ray powder diffraction (XRD) patterns were obtained by X'pert MPD Pro (PANalytical Co), using $\text{Cu-K}\alpha$ radiation (40 kV, 40 mA). The pyrolysis process of the precursor fibers were carried out in TG (Perkin Elmer TGA-7) under a stream of air. The specific surface area was determined according to the Brunauer-Emmett-Teller (BET) method using an ASAP 2020 instrument, and all the samples were of 1 g, respectively, during the BET measurement. The X-ray Photoelectron Spectroscopy (XPS) was carried out by using an Axis Ultra, Kratos (UK) instrument (Al(Mono) X-ray source), while the binding energies were calibrated with respect to the signal for adventitious carbon (binding energy = 284.6 eV). UV-vis absorption spectroscopy (DRS) was recorded using HITACHI UV4100

spectrometer.

2.4. Photocatalytic hydrogen production

In photocatalytic hydrogen production experiment under ultraviolet light ($\lambda < 420\text{ nm}$) irradiation, 0.05 g of the photocatalyst was dispersed in a 50 mL aqueous solution containing 0.25 M Na_2S and 0.35 M Na_2SO_3 which acted as sacrificial agents. In this experiment, a 300 W Xenon lamp with a cutoff filter ($\lambda < 420\text{ nm}$) was employed as the ultraviolet light source. Prior to the irradiation, the system was bubbled with nitrogen for 30 min to remove the air inside and to ensure that the reaction system is under anaerobic conditions. The amount of H_2 evolution was determined on a gas chromatography (Agilent Technologies: 6890N) with TCD equipped with a 5 \AA molecular sieve using N_2 as the carrier gas. Blank experiments revealed that no hydrogen was produced without catalysts added or light irradiation. During the lifetime evaluation process, the reaction system is bubbled with N_2 for 30 min to remove the H_2 inside every 5 h.

2.5. Photoelectrochemical (PEC) measurement

The electrochemical measurements were carried out on a CHI 660D (Shanghai Chenhua Ltd.) electrochemical workstation in a three-electrode system with a platinum wire counter electrode and an Ag/AgCl (saturated KCl) reference electrode, using a concentration of 1 M NaOH aqueous electrolyte under ambient temperature (25°C). The slurry was prepared by mixing 2 mL of ultrapure water, 0.5 mL of isopropanol and 50 μL of perfluorosulfonic acid polymer as well as 3 mg of the as-prepared photocatalyst. The homogeneous slurry was deposited onto the glassy carbon electrode tip (effective area: 0.20 cm^2) and dried at room temperature overnight as the working electrodes. The transient photocurrent response was performed on the electrochemical analyzer using 0.2 V bias voltage under ultraviolet light ($\lambda < 420\text{ nm}$) irradiation. The electrochemical impedance spectra (EIS) were conducted under DC potential of 0.2 V both in the dark and under illumination. A sinusoidal AC voltage of 5 mV amplitude was applied to the electrode with the frequency range of 1000 Hz–0.05 Hz.

3. Results and discussion

As the SEM images shown in Fig. 1a and b, the sample $\text{MT}_2\text{-NF}$ inherited the 1D nanostructures with interconnected flyover-like network from the precursor electrospun fibers (Fig. S2a and b). Typically, the nanofibers with an average diameters of $157.8 \pm 42.0\text{ nm}$ exhibited an excellent continuity (Fig. S2c and d) and a large aspect ratio with lengths ranging up to tens of micrometers. In terms of the sample fabricated by the sol-gel method (Fig. 1c), the $\text{MT}_2\text{-NP}$ presented serious agglomeration of nanoparticles instead of any regular morphologies, similar to those prepared from the traditional solid state reaction. TEM observation revealed that the continuous nanofibers were assembled by packed nano-sized particulates (Fig. 1d). This architecture inevitably resulted in a coarse surface, which together with the agglomeration-free morphology could provide substantial active sites for the photocatalytic reaction. The lattice fringes pertaining to $\text{MT}_2\text{-NF}$ are reflected in the high-resolution TEM (HRTEM) image (Fig. 1e). The distances between adjacent lattices planes were uniformly measured to be 0.27 nm , belonging to the plane (103) of MgTi_2O_5 phase. In addition, the EDS investigation verifies that the sample $\text{MT}_2\text{-NF}$ only consisted of the elements of Mg, Ti and O.

The crystal phases of the samples $\text{MT}_2\text{-NF}$ and $\text{MT}_2\text{-NP}$ were probed by the XRD measurement (Fig. 2). The main diffraction peaks appearing at 2θ of 18.15° , 25.43° , 32.58° , 46.16° and 48.56° in the XRD pattern are properly indexed to those of MgTi_2O_5 (JCPDS No. 35-0792) [18], corresponding to its (200), (101), (230), (430) and (002) facets, respectively. The sharp and high-intensive characteristic peaks implied the high crystallization of the MgTi_2O_5 nanofibers. Notably, signals

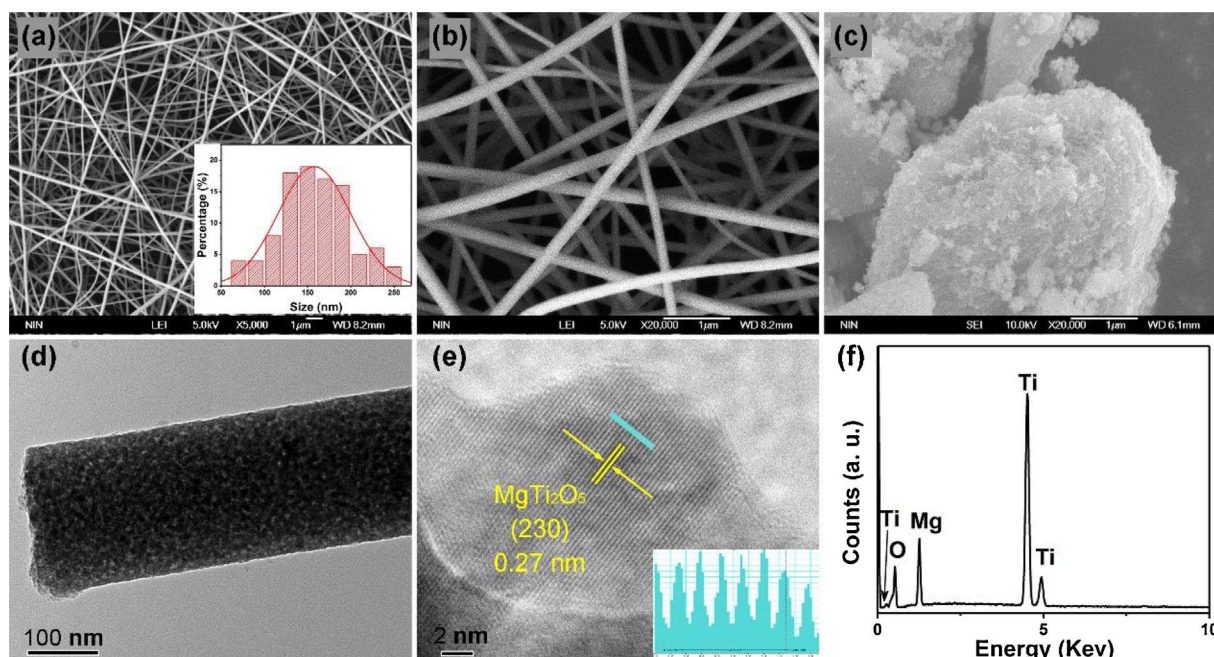


Fig. 1. (a, b) SEM images with different magnification of sample $\text{MT}_2\text{-NF}$, insert is the histogram of diameter distribution; (c) SEM images of sample $\text{MT}_2\text{-NP}$ (c, d) TEM and HRTEM images of sample $\text{MT}_2\text{-NF}$, insert is the line scan of the HRTEM image indicated by the cyan line; (f) EDS spectrum of sample $\text{MT}_2\text{-NF}$.

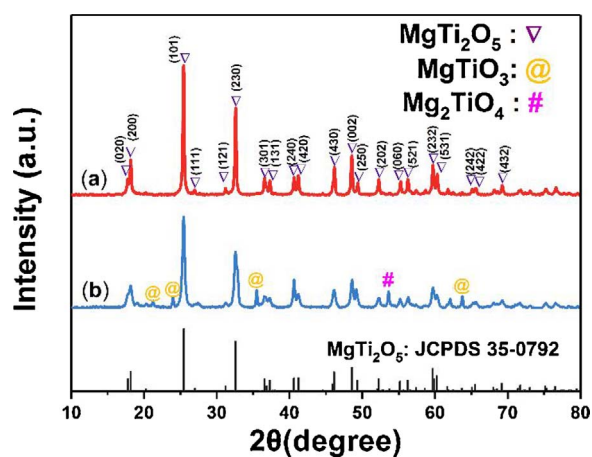


Fig. 2. XRD patterns of sample $\text{MT}_2\text{-NF}$ (a) and $\text{MT}_2\text{-NP}$ (b).

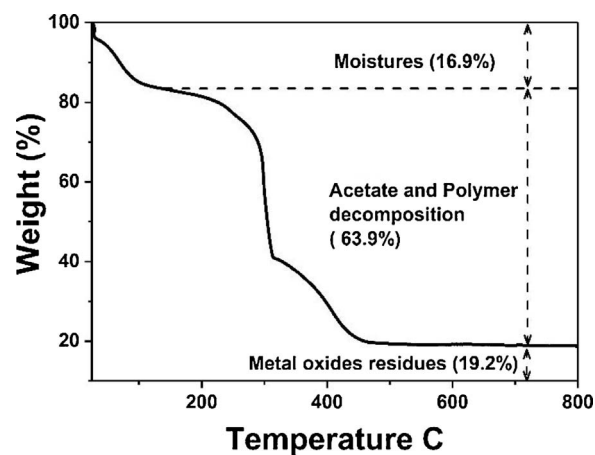


Fig. 3. TG analysis of MgTi_2O_5 precursory nanofibers.

originated from the probable impurities were not detected. By contrast, the sample $\text{MT}_2\text{-NP}$ contained the foreign substances including MgTiO_3 (JCPDS No.04-0694) and Mg_2TiO_4 (JCPDS No.25-1157). Better purity of the electrospun products could be ascribed to the uniform crystallization across the whole sample benefiting from the mesh morphology and the high surface area (shown in Fig. 5), which could improve both mass and heat transfer [35,36]. Amores et al. [35] revealed that the high surface area played a positive role in promoting the process of crystallization and reducing the crystallization temperature. Similarly, Zhang et al. [36] further demonstrated that the crystallization and phase transformation initially occurred on the surface of the materials, so the high surface area and smooth channel of heat transfer were key factors to facilitate the crystal growth, which were also the advantages of the sample $\text{MT}_2\text{-NF}$. On the other hand, the sample $\text{MT}_2\text{-NP}$ with frustrating agglomeration tendency suffered from the inhomogeneous growth of crystal phases, consequently introducing the unpredictable impurities [37].

The pyrolysis process of the sample $\text{MT}_2\text{-NF}$ was recorded through TG analysis. As illustrated in Fig. 3, pyrogenic decomposition of the precursor experienced three dominant steps. The first weight loss of

~16.9% under 200 °C was associated with the evaporation of the solution and the dehydration of crystal water [38]. Obviously, the second remarkable weight loss occurred at the temperature range of 200–500 °C (weight loss ~63.9%) resulted from the decomposition of $\text{Mg}(\text{CH}_3\text{COO})_2$, $\text{Ti}(\text{OC}_4\text{H}_9)_4$ and PVP [39]. Further increasing the temperature was unable to cause any significant weight loss, suggesting the complete decomposition of the organic components before 500 °C. In other words, pure inorganic phases have been prepared under the selected temperature (650 °C) in this work.

XPS was performed to disclose the chemical composition and their valence states of the sample $\text{MT}_2\text{-NF}$ (Fig. 4). The survey scan spectrum in Fig. 4a confirms that Mg, Ti and O coexist in the sample $\text{MT}_2\text{-NF}$, in good agreement with the outcome of EDS. The high-resolution XPS spectrum of the Mg 1s (Fig. 4b) centering at 1303.5 eV indicates the presence of the Mg^{2+} . Fig. 4c indicates that Ti 2p contains two peaks at 458.6 and 464.3 eV, which are ascribed to $\text{Ti } 2p_{3/2}$ and $\text{Ti } 2p_{1/2}$, respectively. The splitting energy is 5.7 eV between these two peaks inferring that the oxidation state of Ti is +4 [27]. As shown in Fig. 4d, there are two peaks in the O 1s fitted XPS spectra. The peaks at 530.1 eV and 532.5 eV are allocated to the crystal lattice oxygen ($\text{O}_{\text{M-O}}$)

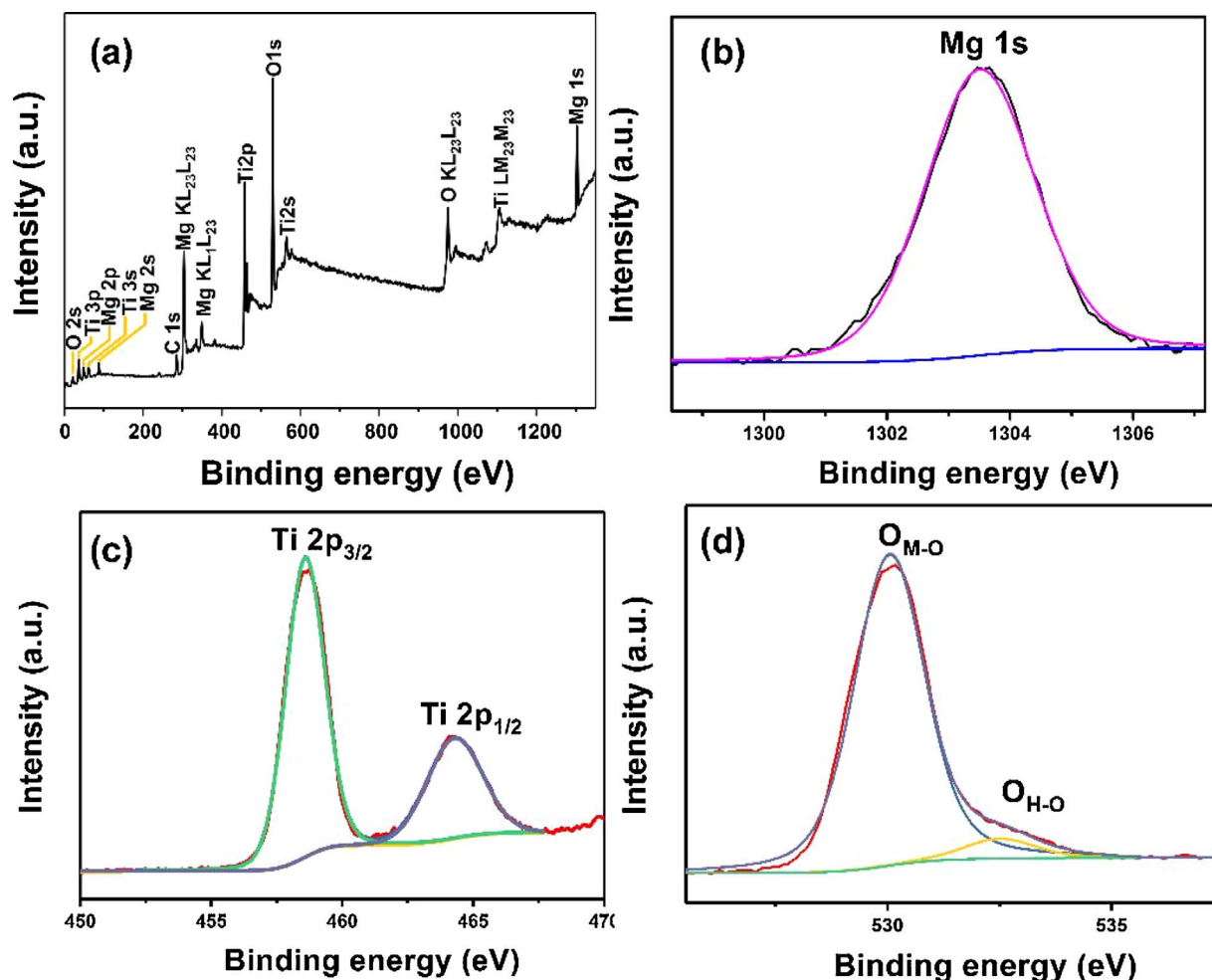


Fig. 4. XPS fully scanned spectra of sample MT₂-NF (a); High-resolution XPS spectrum for Mg 1s (b), Ti 2p (c) and O 1s (d).

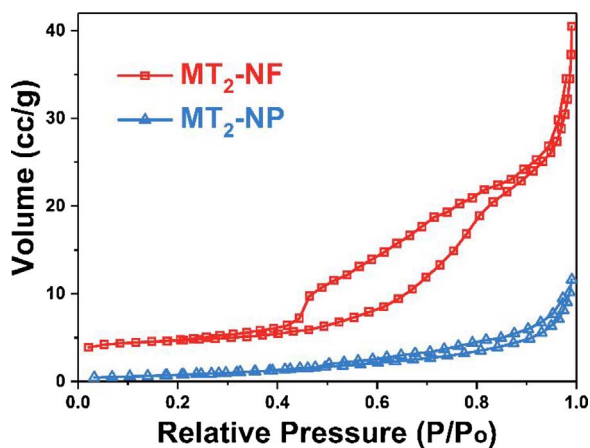


Fig. 5. Nitrogen adsorption-desorption isotherms of the sample MT₂-NF and MT₂-NP.

and surface hydroxyl groups (O_{H-O}) [40].

As shown in Fig. 5, the N₂ adsorption-desorption isotherms obtained from sample MT₂-NF and MT₂-NP followed type IV N₂ sorption isotherms and the corresponding hysteresis loops at high P/P₀ were clearly pertained to type H3 based on the IUPAC classification (Fig. 5) [41], which demonstrate their distinct mesoporous structures. The specific capacitance of sample MT₂-NF ($S_{\text{BET}} = 15.2 \text{ m}^2 \text{ g}^{-1}$) is approximately 5 times larger than that of MT₂-NP ($S_{\text{BET}} = 3.1 \text{ m}^2 \text{ g}^{-1}$). The surface area of the MT₂-NP was close to the commercial MgTiO₅. Higher specific

surface area of sample MT₂-NF could be mainly attributed to the regular morphology. Actually, the surface area has long been accepted as an essential property to enhance the photocatalyst's activity through supplying more reaction sites [42].

The optical properties of the sample MT₂-NF and MT₂-NP were analyzed via the DRS (Fig. 6), and the band gap can be calculated based on the corresponding Tauc plot. As shown, these samples possessed a similar absorption edge at around 365 nm in the UV light region, consistent with the previous reports [15]. The insert was calculated from Tauc's formula: $\alpha(h\nu) = A(h\nu - E_g)^{n/2}$, where α is adsorption

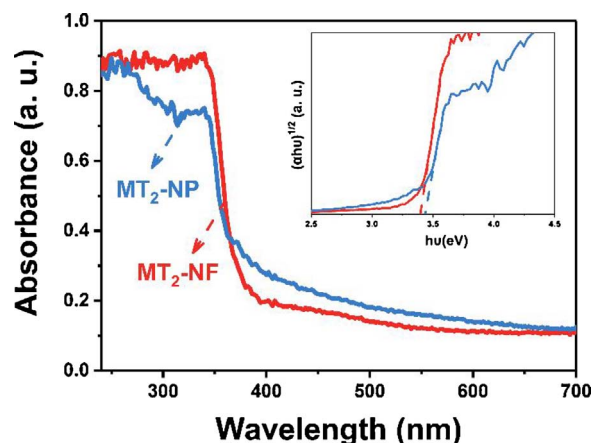


Fig. 6. DRS of the sample MT₂-NF and MT₂-NP; insert is the Tauc plot of the samples.

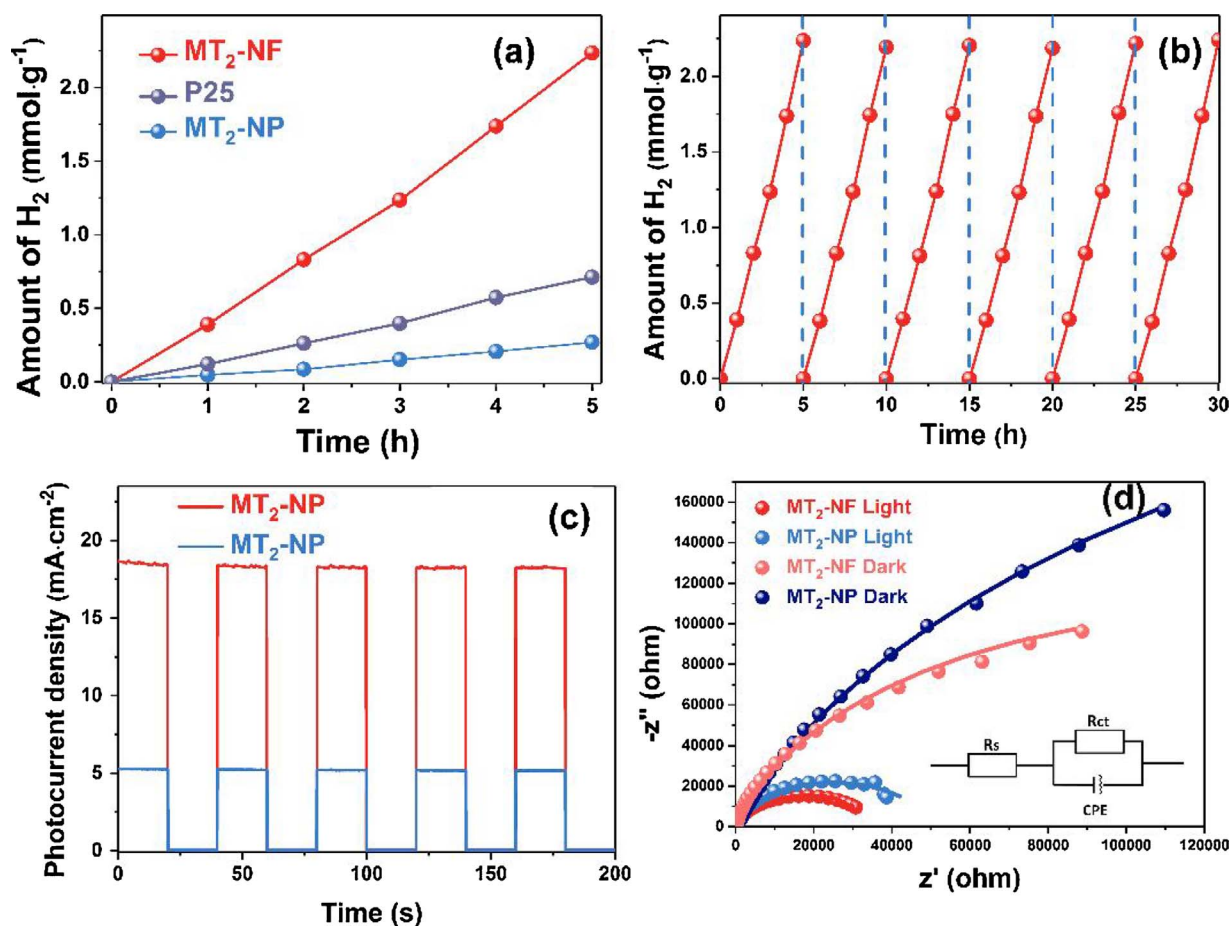


Fig. 7. (a) Photocatalytic H₂ generation efficiencies of MT₂-NF, MT₂-NP and P25; (b) cycle experiments of H₂ evolution for MT₂-NF; (c) The PEC measurements of samples MT₂-NF and MT₂-NP; (d) Amperometric I-t curves with chopped light illumination; (e) EIS curves under UV light and dark conditions, the inset is the equivalent circuit.

coefficient, $h\nu$ is photon energy, A is a constant. The value of n depends on the nature of the transition of the semiconductor, signifying that $n = 1$ stands for direct band gap and $n = 4$ refers to the indirect band gap [43,44]. In this work, $n = 1$ was selected to estimate the band gaps [8]. The band gaps of the samples were measured to be approximately 3.40 and 3.43 eV for the sample MT₂-NF and MT₂-NP, respectively, which match well with the experimental and calculation results [8,27]. Notably, the slight increase about the band gap of sample MT₂-NP was originated from the impurities of MgTiO₃ and Mg₂TiO₄ with higher band gaps [14,45]. These results suggest that the impurity-free MgTi₂O₅ nanofibers fabricated in this work could be used as a photocatalyst under UV light irradiation.

H₂ evolution over samples MT₂-NF, MT₂-NP and P25 under UV light irradiation is posted on Fig. 7a. It is obvious that the sample MT₂-NF delivered the highest H₂ evolution efficiency of 0.45 mmol g⁻¹ h⁻¹ (average over 5 h), which is about four times higher than that of the bench mark P25 (0.14 mmol g⁻¹ h⁻¹). The sample MT₂-NP only demonstrated a low H₂ generation rate of 0.054 mmol g⁻¹ h⁻¹. Moreover, it is important for the photocatalyst to sustain high stability for a long-term, in view of the potentially viable application. As Fig. 7b manifested, MT₂-NF exhibited sustainable photocatalytic performance even after 6 cycles without significant rate loss, conveying that the electrospun product was stable and reusable. Additionally, the sample MT₂-NF could be easily separated from the solution by facile sedimentation as the mixing stopped, creditable to the instinct feature of the large aspect ratio [46].

The PEC properties of samples MT₂-NF and MT₂-NP were evaluated to unlock the underlying reasons why the MT₂-NF possessed the highest photocatalytic activity. To shine light on the photocurrent responses of

the samples, chronoamperometric I-t studies of the samples were conducted during repeated on/off illumination cycles. Both of the samples MT₂-NF and MT₂-NP showed prompt and reproducible photocurrent responses upon each irradiation (Fig. 7c). The transient photocurrent density of MT₂-NF is 18.45 mA cm⁻², which is greatly improved compared with that of MT₂-NP (5.26 mA cm⁻²). Notably, the H₂ evolution efficiency of the sample MT₂-NF is roughly 8 times higher than that of the sample MT₂-NP, while the photocurrent density of sample MT₂-NF is only 3 times higher than that of the sample MT₂-NP. This difference further demonstrated the superiority of the regular 1D nanostructure that the unique 1D mesh structure was propitious for the desorption of generated H₂ from the reaction sites, consequently improving the kinetics of the H₂ evolution process [47].

EIS measurements were executed to crystallize the charge separation and transfer dynamics. Fig. 7d shows that each Nyquist plot of discrete samples consists of a semicircle. The semicircle represents a charge transfer process, as a larger arc radius reflects a larger transfer resistance [48]. The experimental data were fitted using an equivalent circuit model (insert in Fig. 7d), where R_s , R_{ct} , and CPE represent the solution resistance, charge-transfer resistance and double-layer capacitance, respectively [49]. Without light irradiation, samples MT₂-NF and MT₂-NP exhibited similar semicircle Nyquist plots with higher R_{ct} values (Table S1) than those under illumination, suggesting the sluggish electron-transfer kinetics at the surface of the photocatalyst. When turning on the light, R_{ct} values in such two samples obviously decreased, indicating better charge electron transfer efficiency with low charge resistance. The nanofibers ($R_{ct} = 25.9 \times 10^4 \Omega$ at dark and $3.5 \times 10^4 \Omega$ at light, respectively.) demonstrated smaller R_{ct} values (Table S1) than that of nanoparticles ($R_{ct} = 58.3 \times 10^4 \Omega$ at dark and

$5.3 \times 10^4 \Omega$ at light, respectively.) at both dark and illumination conditions, which highlights the more effective electron-transfer kinetics in the one-dimensional samples.

The results of H_2 evolution and the PEC tests jointly corroborated that the sample MT₂-NF demonstrated better photocatalytic activity compared with the sample MT₂-NP. The reasons can be explained in detail as follows: (i) The well-defined 1D nanostructures felicitously solved the contradiction between the long optical penetration depth and shorter migration distance of photogenerated charge carriers [50]. As depicted in Fig. S5, the nanofibers were thick enough along the longitudinal direction allowing adequate light absorption, while the photogenerated e^-/h^+ pairs only migrated a short distance across the radial direction to reach the active sites. Moreover, EIS measurements attested that the 1D architecture rendered lower R_{ct} owing to their less grain boundaries. (ii) The unique mesh topography of the sample MT₂-NF not only entailed higher specific surface areas, but also expedited the gas desorption from the reaction sites by affording abundant empty space among nanofibers, consequently improving kinetics of the H_2 evolution process [51]. (iii) Pure phase also played a positive role in achieving higher photocatalytic activity. Generally, heterojunction was deemed to be conducive to the separation of photoinduced e^-/h^+ pairs. However, the undesigned heterojunctions introduced via the impurities might be buried in the core region apart from the surface due to the serious agglomeration. Zhang et al. found that the unpredictable impurities had an unfavorable tendency to generate recombination centers rather than heterojunctions [26]. (iv) The potential of $MgTi_2O_5$'s conduction band is more negative than that of TiO_2 (P25), meaning that its electrons on conduction band possess stronger reduce ability, which further enhances the thermodynamic driving force for H^+ reduction according to Gerischer theory [52].

Impressively, $MgTiO_3$ and Mg_2TiO_4 nanofibers were also fabricated via electrospinning (Fig. 8). Both electrospun $MgTiO_3$ and Mg_2TiO_4 products exhibited a typical 1D nanostructure (Fig. 8a and d), which were also endowed with favorable continuity (inserts in Fig. 8a and d). In contrast, their counterparts prepared via sol-gel reaction were merely composed of aggregation nanoparticles (Figs. S3a and S4a). The XRD patterns (Fig. 8b and e) and EDS investigations (Fig. S3b and S4b) give an apparent interpretation that neither of the electrospun products

contained any discerned impurities, while the nanoparticle counterparts still had some impurities. In addition, the 1D nanofibers also demonstrated larger surface areas (Fig. S3c and S4c), which were similar to the outcomes of $MgTi_2O_5$. The band gaps of pure $MgTiO_3$ and Mg_2TiO_4 were estimated to be 3.60 eV and 3.95 eV, respectively, in accordance with the previous reports [8,45]. The insignificant difference over band gaps between samples obtained from methods arose from the impurities in the samples obtained from the sol-gel route (Fig. S3d and S4d). More imposingly, the electrospun 1D nanofibers delivered remarkably higher H_2 evolution efficiency in comparison with the nanoparticles (Fig. 8c and f), and the $MgTi_2O_5$ nanofibers exhibited the highest photocatalytic performance prospering from the relatively lower band gap.

Additionally, the $MgTi_2O_5/MgTiO_3$ and $Mg_2TiO_4/MgTiO_3$ heterojunction nanofibers were also prepared via simply changing the molar ratios of Mg to Ti in the precursor. As illustrated in Fig. S6a and d, both of the samples MT₂/MT-NF and MT₂/MT-NF exhibited typical 1D nanostructures with good continuity, similar to the $Mg_xTi_yO_{x+2y}$ electrospun products. The XRD patterns (Fig. S6b and e) further confirmed the successful preparation of composite nanofibers with the target components. It is noteworthy that the sample MT₂/MT-NF delivered higher efficiency on H_2 evolution than the pristine MT₂-NF and MT-NF (Fig. S6c), which is due to the type II band-gap alignment between $MgTi_2O_5$ and $MgTiO_3$ that could promote the photogenerated charge carriers separating [8]. On the other hand, the MT₂/MT-NF failed to enhance the photocatalytic activity (Fig. S6f) because the type I junction constructed between Mg_2TiO_4 and $MgTiO_3$ was not an efficient system for photoinduced electron/hole pairs separating [53]. These results jointly gave strong evidence that the electrospinning technique was able to offer a versatile platform to fabricate a series of pure $Mg_xTi_yO_{x+2y}$ and their heterojunction nanofibers with regular 1D nanostructures. Such 1D nanostructures demonstrate superiority in terms of photocatalytic H_2 generation compared with the traditional nanoparticles.

4. Conclusion

In summary, pure phase $Mg_xTi_yO_{2x+y}$ nanofibers were successfully

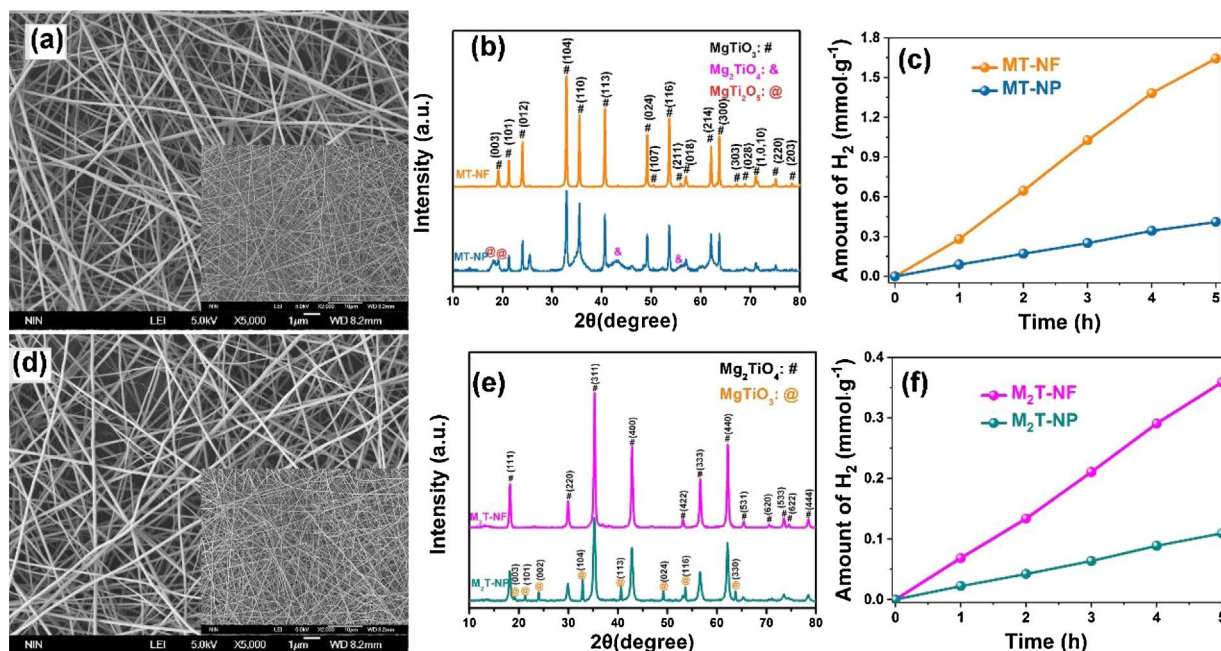


Fig. 8. (a) SEM image of sample MT-NF, insert is the low magnification SEM image; (b) XRD patterns of sample MT-NF and MT-NP; (c) H_2 generation efficiencies of sample MT-NF and MT-NP; (d) SEM image of sample M₂T-NF, insert is the low magnification SEM image; (e) XRD patterns of sample M₂T-NF and M₂T-NP; (f) H_2 generation efficiencies of sample M₂T-NF and M₂T-NP.

prepared via the facile electrospinning method followed by calcination, while the nanoparticle counterparts still contained foreign substances. It underlines the superiority of the electrospinning method in fabricating 1D nanomaterials with regular morphology and high purity. The PEC measurements and photocatalytic H_2 generation efficiency together emphasized that the $Mg_xTi_yO_{2x+y}$ demonstrated superior activities over water splitting under UV light. Particularly, the $Mg_xTi_yO_{2x+y}$ nanofibers processed excellent properties that could synergistically improve the photocatalytic performance, which included well-defined 1D nanostructure, mesh construction, large specific surface areas, pure phase and high conduct band potential. Moreover, the $MgTi_2O_5/MgTiO_3$ and $Mg_2TiO_4/MgTiO_3$ heterogeneous nanofibers were also fabricated, and the $MgTi_2O_5/MgTiO_3$ composite nanofibers possessed enhanced photocatalytic activity benefiting from the type II junctions. Significantly, the electrospun products have proved to be upstanding substrate for direct growth of secondary nanostructures profiting from their porous surface and splendid self-supporting aptitude, which are anticipated to be favorable for assembling more efficient photocatalysts in future.

Acknowledgments

This work was supported by the National Science and Technology Supporting Plan (No.2015BAD16B003), the Fundamental Research Funds for the Central Universities (xj2016052) Natural Science Basic Research Plan in Shaanxi Province of China (2017JM2022) and Natural science fund of Jiangsu Province (BK20170416).

Appendix A. Supplementary data

Supplementary data associated with this article can be found, in the online version, at <https://doi.org/10.1016/j.apcatb.2017.11.062>.

References

- [1] A. Fujishima, K. Honda, Electrochemical photolysis of water at a semiconductor electrode, *Nature* 238 (1972) 37–38.
- [2] N.S. Lewis, Research opportunities to advance solar energy utilization, *Science* 351 (2016) 353.
- [3] T.A. Pham, Y. Ping, G. Galli, Modelling heterogeneous interfaces for solar water splitting, *Nat. Mater.* (2017) 401–408.
- [4] I. Roger, M.A. Shipman, M.D. Symes, Earth-abundant catalysts for electrochemical and photoelectrochemical water splitting, *Nat. Rev. Chem.* 1 (2017) 0003.
- [5] P. Zhang, T. Ochi, M. Fujitsuka, Y. Kobori, T. Majima, T. Tachikawa, Topotactic epitaxy of $SrTiO_3$ mesocrystal superstructures with anisotropic construction for efficient overall water splitting, *Angew. Chem. Int. Ed.* 56 (2017) 5299–5303.
- [6] D.M. Herlihy, M.M. Waagele, X. Chen, C. Pemmaraju, D. Prendergast, T. Cuk, Detecting the oxyl radical of photocatalytic water oxidation at an n- $SrTiO_3$ /aqueous interface through its subsurface vibration, *Nat. Chem.* 8 (2016) 549–555.
- [7] T. Sun, M. Lu, Modification of $SrTiO_3$ surface by nitrogen ion bombardment for enhanced photocatalysis, *Appl. Surf. Sci.* 274 (2013) 176–180.
- [8] Y. Qu, W. Zhou, Y. Xie, L. Jiang, J. Wang, G. Tian, Z. Ren, C. Tian, H. Fu, A novel phase-mixed $MgTiO_3$ - $MgTi_2O_5$ heterogeneous nanorod for high efficiency photocatalytic hydrogen production, *Chem. Commun.* 49 (2013) 8510–8512.
- [9] W. Zhou, F. Sun, K. Pan, G. Tian, B. Jiang, Z. Ren, C. Tian, H. Fu, Well-ordered large-pore mesoporous anatase TiO_2 with remarkably high thermal stability and improved crystallinity: preparation, characterization, and photocatalytic performance, *Adv. Funct. Mater.* 21 (2011) 1922–1930.
- [10] W. Zhou, W. Li, J.Q. Wang, Y. Qu, Y. Yang, Y. Xie, K. Zhang, L. Wang, H. Fu, D. Zhao, Ordered mesoporous black TiO_2 as highly efficient hydrogen evolution photocatalyst, *J. Am. Chem. Soc.* 136 (2014) 9280–9283.
- [11] X. Sun, Y. Xie, F. Wu, H. Chen, M. Lv, S. Ni, G. Liu, X. Xu, Photocatalytic hydrogen production over chromium doped layered perovskite Sr_2TiO_4 , *Inorg. Chem.* 54 (2015) 7445–7453.
- [12] L. Cheng, P. Liu, S.-X. Qu, L. Cheng, H. Zhang, Microwave dielectric properties of Mg_2TiO_4 ceramics synthesized via high energy ball milling method, *J. Alloys Compd.* 623 (2015) 238–242.
- [13] U. Ullah, W.F.F.W. Ali, M.F. Ain, N.M. Mahyuddin, Z.A. Ahmad, Design of a novel dielectric resonator antenna using $MgTiO_3$ - $CoTiO_3$ for wideband applications, *Mater. Des.* 85 (2015) 396–403.
- [14] N. Zhang, Y. Qu, K. Pan, G. Wang, Y. Li, Synthesis of pure phase $Mg_{1.2}Ti_{1.8}O_5$ and $MgTiO_3$ nanocrystals for photocatalytic hydrogen production, *Nano Res.* 9 (2016) 726–734.
- [15] L. Meng, Z. Ren, W. Zhou, Y. Qu, G. Wang, $MgTiO_3/MgTi_2O_5/TiO_2$ heterogeneous belt-junctions with high photocatalytic hydrogen production activity, *Nano Res.* 10 (2016) 295–304.
- [16] R. Jin, W. Gao, J. Chen, H. Zeng, F. Zhang, Z. Liu, N. Guan, Photocatalytic reduction of nitrate ion in drinking water by using metal-loaded $MgTiO_3$ - TiO_2 composite semiconductor catalyst, *J. Photochem. Photobiol. A* 162 (2004) 585–590.
- [17] M.A. Reddy, M.S. Kishore, V. Pralong, V. Caignaert, U.V. Varadaraju, B. Raveau, Synthesis and lithium insertion into nanophase $MgTi_2O_5$ with pseudo-brookite structure, *Chem. Mater.* 20 (2008) 2192–2197.
- [18] F. Xie, Y. Deng, Y. Xie, H. Xu, G. Chen, Ultra-small nanoparticles of $MgTi_2O_5$ embedded in carbon rods with superior rate performance for sodium ion batteries, *Chem. Commun.* 51 (2015) 3545–3548.
- [19] S. Chakrabarti, K. Biswas, DFT study of Mg_2TiO_4 and Ni doped $Mg_{1.5}Ni_{0.5}TiO_4$ as electrode material for Mg ion battery application, *J. Mater. Sci.* 52 (2017) 10972–10980.
- [20] X. Wang, J. Cai, Y. Zhang, L. Li, L. Jiang, C. Wang, Heavy metal sorption properties of magnesium titanate mesoporous nanorods, *J. Mater. Chem. A* 3 (2015) 11796–11800.
- [21] Y.-D. Ho, C.-H. Su, C.-L. Huang, A. Srivastava, Intense red photoluminescence emission of sol-gel-derived nanocrystalline Mg_2TiO_4 thin films, *J. Am. Ceram. Soc.* 97 (2014) 358–360.
- [22] D.K. Roh, S.J. Kim, H. Jeon, J.H. Kim, Nanocomposites with graft copolymer-templated mesoporous $MgTiO_3$ perovskite for CO_2 capture applications, *ACS Appl. Mater. Interfaces* 5 (2013) 6615–6621.
- [23] W. Dong, B. Li, Y. Li, X. Wang, L. An, C. Li, B. Chen, G. Wang, Z. Shi, General approach to well-defined perovskite $MTiO_3$ ($M = Ba, Sr, Ca, \text{ and } Mg$) nanostructures, *J. Phys. Chem. C* 115 (2011) 3918–3925.
- [24] M. Llusar, E. García, M.T. García, V. Esteve, C. Gargori, G. Monrós, Synthesis and coloring performance of Ni-geikielite (Ni, Mg)/ TiO_3 yellow pigments: effect of temperature, Ni-doping and synthesis method, *J. Eur. Ceram. Soc.* 35 (2015) 3721–3734.
- [25] Y. Suzuki, T.S. Suzuki, Y. Shinoda, K. Yoshida, Uniformly porous $MgTi_2O_5$ with narrow pore-size distribution: XAFS study, improved in situ synthesis, and new in situ surface coating, *Adv. Eng. Mater.* 14 (2012) 1134–1138.
- [26] N. Zhang, K. Zhang, W. Zhou, B. Jiang, K. Pan, Y. Qu, G. Wang, Pure phase orthorhombic $MgTi_2O_5$ photocatalyst for H_2 production, *RSC Adv.* 5 (2015) 106151–106155.
- [27] M.A. Ehsan, R. Naeem, V. McKee, A.S. Hakeem, M. Mazhar, $MgTi_2O_5$ thin films from single molecular precursor for photoelectrochemical water splitting, *Sol. Energy Mater. Sol. Cells* 161 (2017) 328–337.
- [28] P. Kapoor, S. Uma, S. Rodriguez, K. Klabunde, Aerogel processing of MTi_2O_5 ($M = Mg, Mn, Fe, Co, Zn, Sn$) compositions using single source precursors: synthesis, characterization and photocatalytic behavior, *J. Mol. Catal. A: Chem.* 229 (2005) 145–150.
- [29] L. Mai, X. Tian, X. Xu, L. Chang, L. Xu, Nanowire electrodes for electrochemical energy storage devices, *Chem. Rev.* 114 (2014) 11828–11862.
- [30] B. Li, Y. Hao, B. Zhang, X. Shao, L. Hu, A multifunctional noble-metal-free catalyst of CuO/TiO_2 hybrid nanofibers, *Appl. Catal. A* 531 (2017) 1–12.
- [31] P.P. Das, A. Roy, M. Tathavadekar, P.S. Devi, Photovoltaic and photocatalytic performance of electrospun Zn_2SnO_4 hollow fibers, *Appl. Catal. B* 203 (2017) 692–703.
- [32] K. Guo, Z. Liu, C. Zhou, J. Han, Y. Zhao, Z. Liu, Y. Li, T. Cui, B. Wang, J. Zhang, Fabrication of TiO_2 nano-branched arrays/ Cu_2S composite structure and its photoelectric performance, *Appl. Catal. B* 154 (2014) 27–35.
- [33] S. Peng, G. Jin, L. Li, K. Li, M. Srinivasan, S. Ramakrishna, J. Chen, Multi-functional electrospun nanofibers for advances in tissue regeneration, energy conversion & storage, and water treatment, *Chem. Soc. Rev.* 45 (2016) 1225–1241.
- [34] A. Greiner, J.H. Wendorff, Electrospinning: a fascinating method for the preparation of ultrathin fibers, *Angew. Chem. Int. Ed.* 46 (2007) 5670–5703.
- [35] J.M.G. Amores, V.S. Escribano, Anatase crystal growth and phase transformation to rutile in high-area TiO_2 , MoO_3 - TiO_2 and other TiO_2 -supported oxide catalytic systems, *J. Mater. Chem.* 5 (1995) 1245–1249.
- [36] H. Zhang, J.F. Banfield, New kinetic model for the nanocrystalline anatase-to-rutile transformation revealing rate dependence on number of particles, *Am. Mineral.* 84 (1999) 528–535.
- [37] Y. Zhao, Q. Lai, H. Zeng, Y. Hao, Z. Lin, $Li_4Mn_5O_{12}$ prepared using L-lysine as additive and its electrochemical performance, *Ionics* 19 (2013) 1483–1487.
- [38] W.T. Koo, S.J. Choi, S.J. Kim, J.S. Jang, H.L. Tuller, I.D. Kim, Heterogeneous sensitization of metal-organic framework driven metal@metal oxide complex catalysts on an oxide nanofiber scaffold toward superior gas sensors, *J. Am. Chem. Soc.* 138 (2016) 13431–13437.
- [39] A.V. Radhamani, K.M. Shareef, M.S. Rao, $ZnO@MnO_2$ core-shell nanofiber cathodes for high performance asymmetric supercapacitors, *ACS Appl. Mater. Interfaces* 8 (44) (2016) 30531–30542.
- [40] G. Yang, L. Wang, J. Wang, W. Yan, Fabrication and formation mechanism of Li_2MnO_3 ultrathin porous nanobelts by electrospinning, *Ceram. Int.* 43 (2017) 71–76.
- [41] J. Wang, G. Yang, L. Wang, W. Yan, Synthesis of one-dimensional $NiFe_2O_4$ nanostructures: tunable morphology and high-performance anode materials for Li ion batteries, *J. Mater. Chem. A* 4 (2016) 8620–8629.
- [42] L. Qin, X. Pan, L. Wang, X. Sun, G. Zhang, X. Guo, Facile preparation of mesoporous $TiO_2(B)$ nanowires with well-dispersed Fe_2O_3 nanoparticles and their photochemical catalytic behavior, *Appl. Catal. B* 150–151 (2014) 544–553.
- [43] J. Tauc, Optical properties and electronic structure of amorphous Ge and Si, *Mater. Res. Bull.* 3 (1968) 37–46.
- [44] G. Yang, W. Yan, Q. Zhang, S. Shen, S. Ding, One-dimensional CdS/ZnO core/shell nanofibers via single-spinneret electrospinning: tunable morphology and efficient photocatalytic hydrogen production, *Nanoscale* 5 (2013) 12432–12439.

- [45] M.M. Medić, M. Vasić, A.R. Zarubica, L.V. Trandafilović, G. Dražić, M.D. Dramićanin, J.M. Nedeljković, Enhanced photoredox chemistry in surface-modified Mg_2TiO_4 nano-powders with bidentate benzene derivatives, *RSC Adv.* 6 (2016) 94780–94786.
- [46] Z. Zhang, C. Shao, X. Li, Y. Sun, M. Zhang, J. Mu, P. Zhang, Z. Guo, Y. Liu, Hierarchical assembly of ultrathin hexagonal SnS_2 nanosheets onto electrospun TiO_2 nanofibers: enhanced photocatalytic activity based on photoinduced interfacial charge transfer, *Nanoscale* 5 (2013) 606–618.
- [47] C. Liu, P.-C. Hsu, H.-W. Lee, M. Ye, G. Zheng, N. Liu, W. Li, Y. Cui, Transparent air filter for high-efficiency $\text{PM}_{2.5}$ capture, *Nat. Commun.* 6 (2015) 6205.
- [48] F. Lei, Y. Sun, K. Liu, S. Gao, L. Liang, B. Pan, Y. Xie, Oxygen vacancies confined in ultrathin indium oxide porous sheets for promoted visible-light water splitting, *J. Am. Chem. Soc.* 136 (2014) 6826–6829.
- [49] D. Hou, W. Zhou, X. Liu, K. Zhou, J. Xie, G. Li, S. Chen, Pt nanoparticles/ MoS_2 nanosheets/carbon fibers as efficient catalyst for the hydrogen evolution reaction, *Electrochim. Acta* 166 (2015) 26–31.
- [50] X. Fan, T. Wang, B. Gao, H. Gong, H. Xue, H. Guo, L. Song, W. Xia, X. Huang, J. He, Preparation of the TiO_2 /graphitic carbon nitride core-shell array as a photoanode for efficient photoelectrochemical water splitting, *Langmuir* 32 (2016) 13322–13332.
- [51] R. Zhang, C. Liu, P.-C. Hsu, C. Zhang, N. Liu, J. Zhang, H.R. Lee, Y. Lu, Y. Qiu, S. Chu, Nanofiber air filters with high-temperature stability for efficient $\text{PM}_{2.5}$ removal from the pollution sources, *Nano Lett.* 16 (2016) 3642–3649.
- [52] H. Gerischer, The impact of semiconductors on the concepts of electrochemistry, *Electrochim. Acta* 35 (1990) 1677–1699.
- [53] S.J.A. Moniz, S.A. Shevlin, D.J. Martin, Z.-X. Guo, J. Tang, Visible-light driven heterojunction photocatalysts for water splitting – a critical review, *Energy Environ. Sci.* 8 (2015) 731–759.